ORIGINAL ARTICLE

Exploration of microstructure characteristics and mechanical behaviors of thermal-damaged argillaceous sandstone via LF-NMR and μ-CT technologies

Shi Liu · **Zhe Huang**

Abstract The effect of high temperature on the microstructure and mechanical behavior of rocks is a fundamental issue relevant to the exploitation of underground oil and gas resources, underground disposal of highly radioactive nuclear waste, and the development of geothermal energy. In this study, samples of argillaceous sandstone are subjected to high-temperature treatments (i.e., 25 ℃, 300 ℃, 600 ℃, 900 ℃, 1000 ℃, and 1200 ℃) followed by a series of uniaxial compression tests. Qualitative and quantitative analyses of the microscopic structures of the samples are carried out using scanning electron microscopy (SEM), low-field nuclear magnetic resonance (LF-NMR) and micron-scale computed tomography (μ-CT). Thermal damage defined by porosity is established and used to describe the evolution of rock damage over the temperature increase. After the high-temperature treatments, LF-NMR results indicate that small and medium pores consistently dominate the structure, with pore volumes of up to 98.8% to 100%. μ-CT test results show that the distribution frequency of medium pores is 16.5–28.3% and that of large pores is 71.7–83.5%. The μ-CT porosity ranges from 11.1 to 15.2% and the LF-NMR porosity ranges from 18.9 to 26.3%. When subjected to the same temperature, the μ-CT porosity is generally smaller than the LF-NMR porosity. When the temperature is increased, the peak stress and elastic modulus increases first and then decreases, while the peak strain decreases first and then increases. Test results of three mechanical parameters all indicate that 300 ℃ is probably the threshold temperature of the test rock type, and the SEM, LF-NMR and μ-CT test results confirm this temperature. The relationship between thermal damage and temperature suggests that the argillaceous sandstone evolves through strengthening, damage derivation, and damage development as applied temperature increases.

Highlights

- SEM, LF-NMR and μ-CT were combined to investigate microstructure of thermal-damaged rock.
- 300 ℃ is the threshold temperature of argillaceous sandstone under uniaxial compression tests.
- A thermal damage evolution equation was established defined by the μ-CT porosity and LF-NMR porosity.

S. Liu (✉)
State Key Laboratory for GeoMechanics and Deep Underground Engineering, China University of Mining and Technology, Xuzhou, Jiangsu 221116, People's Republic of China
e-mail: fzdyhtbdy@126.com

S. Liu · Z. Huang
Aviation Engineering School, Air Force Engineering University, Xi'an, Shaanxi 710038, People's Republic of China

1 Introduction

Geology and rock mechanics information are dependent on accurate pore structure analyses, and high-temperature conditions create significant challenges in the exploration of rock microstructure characteristics and mechanical behaviors (Zhang et al. 2020). Such conditions are relevant to the development and utilization of geothermal resources, the underground storage of nuclear waste, and the underground gasificon of coal. Hence the relevance of the study of the effect of high-temperature treatments on the microstructure characteristics and mechanical behaviors of rocks. The microscopic structure of rock changes under the action of temperature and load (Pathiranagei et al. 2021; Wu et al. 2021a; Zhao et al. 2017), causing the development, growth and extension of micro-defects dispersed in various forms, eventually causing rock instability and failure due to macroscopic cracks (Liu et al. 2018; Ma et al. 2021; Martinez-Ibanez et al. 2021; Sun et al. 2021). With the continuous update of test loading equipment and microscopic detection technology, it has been found that the mechanical response of rock is the macroscopic reflection of changes to the internal microscopic structure (Ding et al. 2020; Li et al. 2021; Liang et al. 2021; Sun et al. 2021). This provides a different perspective for the analysis of the influence of high-temperature on the physical and mechanical properties of rock.

Pores occur naturally in various rock substrates and form the main body of the rock together with its skeleton (Hao et al. 2022; Wang et al. 2022). Pore structure characteristics include the shape, size, distribution, and interconnectivity of the pores and tunnels in the rock (Katika et al. 2018; Xiao et al. 2021; Zhou et al. 2018), and are important in regards to the macro-mechanical characteristics of rock materials (Jiang et al. 2020). In porous rock media, the complex geological environment leads to the complex pore structure, including large-scale ranges, diverse types, and discrete distributions (Li et al. 2018; Zhu et al. 2018). The joint action of primary tectonic action conditions and secondary destructive diagenesis conditions create a large number of micron and nanometer pores. Pore structure evolution characteristics tend to be more complex and variable under high-temperature (up to thousands of degrees Celsius) environments compared to under lower-temperature conditions (Li et al. 2020; Liu and Xu 2015; Kumari et al. 2018). Typical studies include but are not limited to the following: Pathiranagei et al. (2021) conducted a series of laboratory experiments on Beaudesert sandstone, Jimboomba sandstone, basalt and argillite at temperatures ranging from 25 to 800 ℃, and explored the influence of high temperature on rock engineering properties from the perspectives of porosity, mineral composition, threshold temperature, etc. Wu et al. (2021a) investigated the influence of high temperature effect on granite porosity, P-wave velocity, tensile strength and microstructure in order to study the influence of the heat released from the decay of nuclides on the physical and mechanical properties of the surrounding rock of high-level radioactive waste repository. Xu et al. (2021) analyzed the dynamic mechanical properties and hydrothermal damage effect of granite under the condition of 25–150 ℃ water immersion with the help of Hopkinson pressure bar and nuclear magnetic resonance instrument. Kahraman (2022) taking the prediction of high temperature exposure effect of rock mass as the engineering background, emphatically discussed the physical mechanics and microstructure characteristics of Turkish granite after undergoing high temperature and different cooling methods. Li et al. (2022) taking granite and sandstone as objects, explored the microstructure and crack evolution process of rocks under the influence of different temperature gradients and cooling modes.

Advancements in testing methods and techniques have gradually expanded microscopic characteristic analyses from being qualitative to being quantitative. Microscopic characteristics are typically studied using non-image analysis or image analysis testing principles. Non-image analyses have included high-pressure mercury injection tests (Chang et al. 2020; Lyu et al. 2021), gas adsorption tests (Liu et al. 2019; Yuan et al. 2021) and low-field nuclear magnetic resonance tests (Adeyilola et al. 2020; Habina et al. 2017; Hashan et al. 2022; Romero-Sarmiento et al. 2017), etc. The basic principle of non-image analysis is to invert the characteristic parameters of pore structure by obtaining the volume or mass of a fluid or gas injected into

pores. However, this method does not directly display spatial information describing the pore structure. Image analysis methods include micron-scale computed tomography (Bandara et al. 2021; Ebadi et al. 2021; Kim et al. 2020; Yu et al. 2021), small-angle X-ray scattering (Zhao et al. 2020b, 2019), and scanning electron microscopy (Das et al. 2021; Wang and Sun 2021). The basic principle of image analysis methods is to directly observe pore structure characteristics such as size, connectivity, and other relevant parameters.

The accuracy of quantitative microscopic structure measurements is directly related to the test methods used to gather them. Different test methods can cause large differences between measurement results, and different methods have unique scopes of application. There are currently many uncertainties and unknowns regarding the evolution of microscopic structure in rocks under the influence of high-temperature, and there is a general lack of research on the subject. In this study, argillaceous sandstone from the Leshan Area, Sichuan Province, China, is taken as the research object. Uniaxial compression tests are performed on samples of this sandstone subjected to a range of temperatures (25 ℃, 300 ℃, 600 ℃, 900 ℃, 1000 ℃, and 1200 ℃) to explore the threshold temperature of key mechanical parameters. SEM is employed to investigate the effect of high temperatures on the microstructure of the argillaceous sandstone from a qualitative perspective. LF-NMR and high-resolution μ-CT system analyses are used to quantitatively characterize the pore structural multi-scale characteristics of the argillaceous sandstone after thermal damage has occurred. The evolution of pore size distribution and porosity with temperature is analyzed, and the difference between the results of the two image-based analyses are discussed. Thermal damage variables are examined using porosity as the reference quantity and the mechanism causing the evolution of thermal damage is investigated. The exploration of the mechanism by which high temperature effects the nonlinear behavior of argillaceous sandstone, using macro-mechanical tests and micro-imaging at different scales, contributes to the further understanding and evaluation of the high-temperature response of rocks.

2 Methodology

The experimental design consisted of two principal components: uniaxial compression tests to study the effect of temperature on the mechanical parameters of rock, and microscopic tests to study the effect of temperature on rock microstructure. The test process and test equipment are summarized in Fig. 1. Test samples were taken from argillaceous sandstone from the Leshan Area, Sichuan Province, China. Burial depths were between 500 and 800 m below the surface. The appearance of this sandstone is dark red. The sandstone had an average density measured in the rock's natural state of 2.28 g/cm^3, an average p-wave velocity of 3000–3500 m/s and a weighing porosity of 19.6%. The unheated rock had a uniaxial compressive strength (measured using a standard cylinder sample $\Phi 50 \times 100$ mm) of 35–40 MPa.

The rock samples were processed into cylinders. All samples had a surface parallelism value less than 0.05 mm, and a surface flatness less than 0.02 mm. Three different sizes were used: (1) Φ 50×100 mm for uniaxial compression tests. This size met the requirements of the International Society of Rock Mechanics (ISRM 2007). Crushed rock fragments with suitable sizes were selected from the results of the uniaxial compression tests for subsequent SEM observation; (2) Φ 25×50 mm for the LF-NMR analyses. This size was determined by the size of the nuclear magnetic testing instrument coil; (3) Φ 5×10 mm for the μ-CT analyses. This size was based on existing rock core-drilling sampling technology and ensured a minimum size needed for accurate analysis. All processed rock samples were collected from the same batch of blocks from the same place of origin. The samples were screened through ultrasonic longitudinal wave velocity detection to ensure their uniformity. Sample nomenclature followed a code consisting of three parts, X-Y-Z, where X refers to the analysis type used on the sample, Y the temperature treatment applied to the sample, and Z the number of the sample replicate (three in all). Code values are as follows. X: A—uniaxial compression test; B—LF-NMR analysis; C—μ-CT analysis. Y: 1–25 ℃; 2–300 ℃; 3–600 ℃; 4–900 ℃; 5—1000℃; 6–1200 ℃. Z: 1, 2, or 3. Each sample was heated in a high-temperature furnace to the target treatment temperature, held at this temperature for 1 to 3 h and then
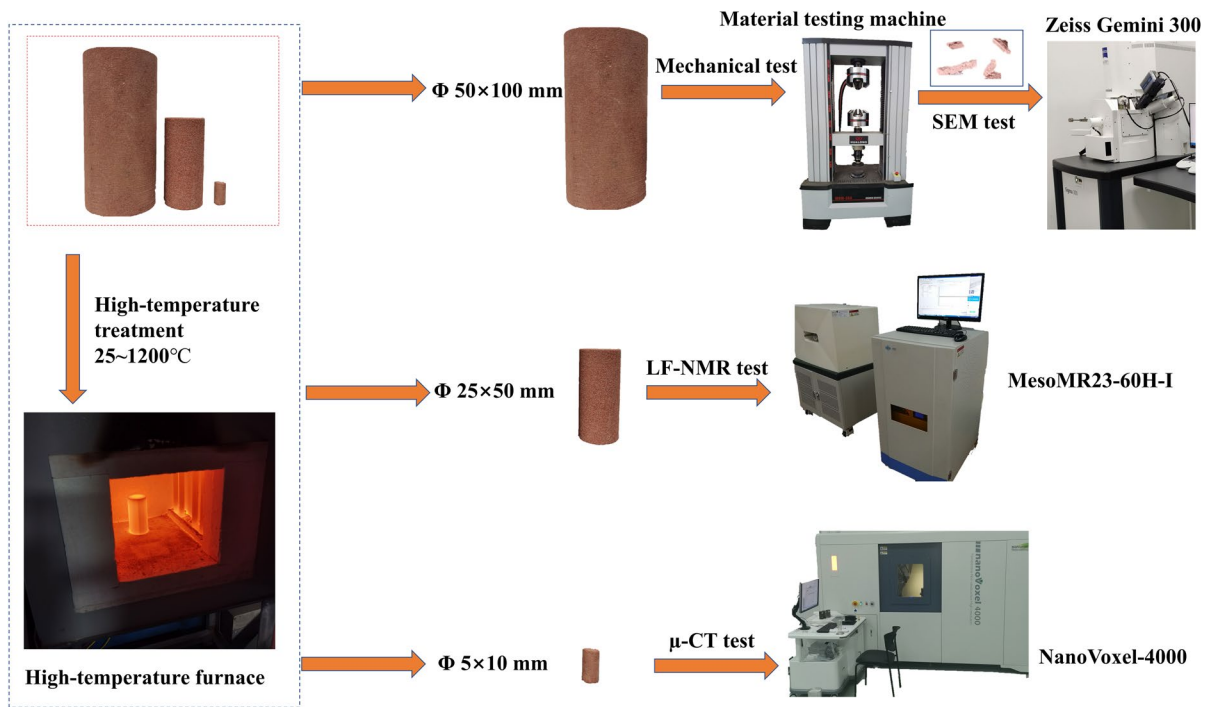
Fig. 1 Overall technical roadmap for experimental design

naturally cooled. The heating rate used was 10 ºC/min. The time each sample was held at the treatment temperature varied depending on the sample size.

Mechanical tests were then carried out using a rock mechanics testing machine. The displacement control method was used to load a sample until it was damaged. SEM imaging was then used to analyze the microstructure of high-temperature argillaceous sandstone at the 10^1–10^2 µm scale. LF-NMR and µ-CT methods were then combined to investigate the pore development characteristics of thermally damaged argillaceous sandstone, thus resolving the shortcomings of either test method. The LF-NMR test equipment used was the MesoMR23-60H-I. A heat-treated rock sample was first placed in a vacuum drying oven until its weight difference between two adjacent time points was less than 0.1%, when it was considered to be completely dry. The completely dried sample was then subjected to vacuum pressurization and water saturation for 24 h until the sample no longer absorbed water and was regarded as completely saturated. Finally, LF-NMR was conducted to test the T_2 spectrum transverse relaxation time of the thermally damaged rock sample. The µ-CT test equipment used

was a NanoVoxel-4000 series high-resolution X-ray three-dimensional (3D) microscope. Each sample was scanned using 360° rotating µ-CT in all directions. The resulting images were subjected to a series of digital image processes (i.e., image enhancement, image filtering, image segmentation and data reconstruction) in order to obtain high-resolution 3D digital images of the rock core for visual pore structure analysis. Finally, Volume Graphics Studio MAX software was used to quantitatively extract and analyze micro-pore structure data.

3 Results

3.1 Mechanical properties

Typical stress–strain curves of the argillaceous sandstone under uniaxial compression load after being subjected to different high-temperature treatments are presented in Fig. 2, and relevant associated mechanical properties are summarized in Table 1. Figure 3 presents the relationship between uniaxial compression mechanical parameters and treatment
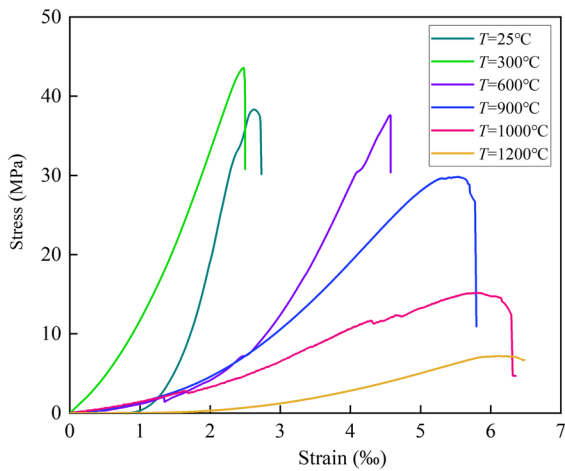
Fig. 2 Typical stress–strain curves of argillaceous sandstone specimens subjected to high-temperature treatments

temperature. Treatment temperature clearly has a certain influence on the shape of the stress–strain curve. From normal temperature (25 ℃) to 600 ℃, the brittle characteristics of the rock sample are obvious, and this stage can be regarded as a typical brittle failure

stage. From 900 to 1000℃, the brittle characteristics gradually weaken while plastic characteristics gradually appear, and this stage can be regarded as a transition stage from brittle to plastic. At 1200 ℃, the sample presents obvious plastic failure characteristics. At this time, after reaching a peak stress, the sample still has a certain bearing capacity with the increase of strain. The brittle-plastic rock failure transition is a typical high-temperature mechanical response of rock under thermal–mechanical coupling (Ranjith et al. 2012; Sun et al. 2015; Zhao et al. 2020a). The changes seen in strength characteristics (Fig. 3) were as follows. When the treatment temperature was increased from normal temperature to 300 ℃, the peak stress did not decrease but increased, indicating that the high-temperature not only did not weaken the bearing capacity of the rock, but improved the effective bearing area by evaporating water (Liu and Xu 2014; Wang et al. 2020), and filling some of the pores. With a further increase of treatment temperature from 300 to 1200 ℃, the peak stress gradually decreased. This suggests that 300℃ treatment provides the extreme value of peak stress. 300 ℃ may not be the exact extreme point due to the coarse

Table 1 Statistics of uniaxial compression test results

| Sample no	Temperature T (℃)	Peak stress (MPa)	Average peak stress (MPa)	Peak strain (‰)	Average peak strain (‰)	Elastic modulus (GPa)	Average elastic modulus (GPa)
A-1–1	25	40.10	38.3	2.66	2.63	22.11	21.03
A-1–2	25	38.46		2.64		22.18	
A-1–3	25	36.34		2.59		18.79	
A-2–1	300	42.19	43.58	2.52	2.48	25.98	24.80
A-2–2	300	43.71		2.50		22.11	
A-2–3	300	44.84		2.44		26.29	
A-3–1	600	36.28	37.59	4.60	4.57	18.20	16.59
A-3–2	600	37.79		4.58		14.50	
A-3–3	600	38.70		4.52		17.07	
A-4–1	900	31.10	29.81	5.78	5.55	9.58	8.02
A-4–2	900	29.75		5.56		7.51	
A-4–3	900	28.58		5.30		6.96	
A-5–1	1000	14.01	15.13	6.00	5.82	5.87	3.69
A-5–2	1000	15.20		5.84		2.98	
A-5–3	1000	16.18		5.63		2.23	
A-6–1	1200	8.90	7.182	6.36	6.22	2.10	1.52
A-6–2	1200	6.98		6.28		0.98	
A-6–3	1200	5.67		6.01		1.47	

(a)

(b)

(c)
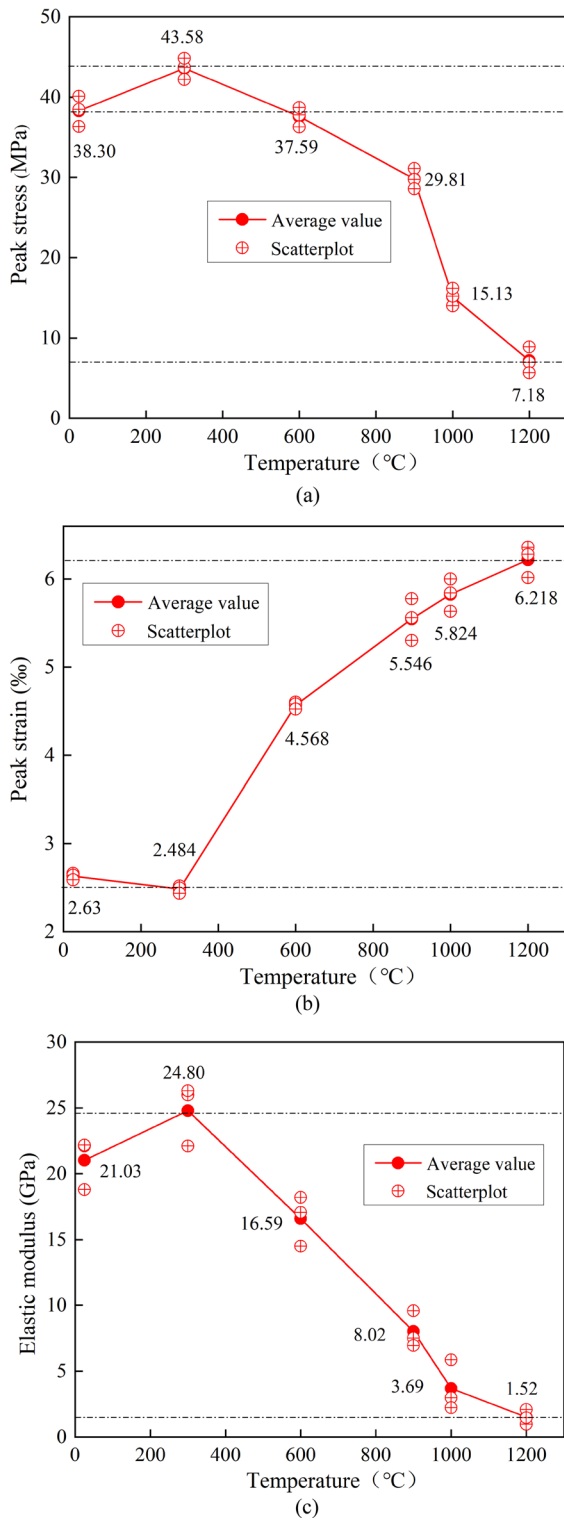
Fig. 3 Effect of temperature on the strength and deformation parameters of argillaceous sandstone specimens under uniaxial compression: **a** Peak stress; **b** Peak strain; **c** Elastic modulus

resolution of the high-temperature heating intervals, but it is certain that the threshold temperature of the uniaxial compressive strength is around 300 ºC. This threshold temperature is consistent with the results of previous studies, although the threshold temperatures for different rock types and heating levels differ (Kang et al. 2021; Ma et al. 2020; Meng et al. 2021; Wu et al. 2021b).

The changes seen in the deformation characteristics (Fig. 3) were as follows. With the increase of treatment temperature, the peak strain first decreased and then increased, and the elastic modulus first increased then decreased. Although the evolution directions of the two deformation indicators were opposite, the common point is that both of them exhibited a turning point at 300 °C, which once again confirms the assumption that 300 °C is the threshold temperature of argillaceous sandstone. Not only does the strength have a threshold temperature, but the deformation also has a threshold temperature, and the two threshold temperatures are very close. Hence the uniaxial compression test results demonstrate that argillaceous sandstone has a threshold temperature, but this is only a macroscopic mechanical result, and the effect of high-temperature treatment on rock microstructure needs to be further understood from the perspective of the micro-scale.

3.2 Analysis of SEM results

Figure 4 presents a schematic diagram of part of the microstructure of argillaceous sandstone at normal temperature. Rock samples at normal temperature contain a lot of argillaceous clay minerals (Fig. 4a). The arrangement of mineral particles is relatively random, with no fixed direction, and there are many pores with huge differences in scale between them. The complex microstructure of the rock sample is formed of various kinds of mineral particles by alternately connecting with each other. Many particles are attached with reticular cemented substances on the surface. Region A in Fig. 4a is magnified by 2000 times and shown in Fig. 4b, and Region B is magnified to 10,000 times and shown in Fig. 4c. A large number of micron-nano pores are found densely packed between the reticular cemented materials. The scattered accumulation Region C in Fig. 4a is magnified 2000 times and presented in Fig. 4d. Here, there
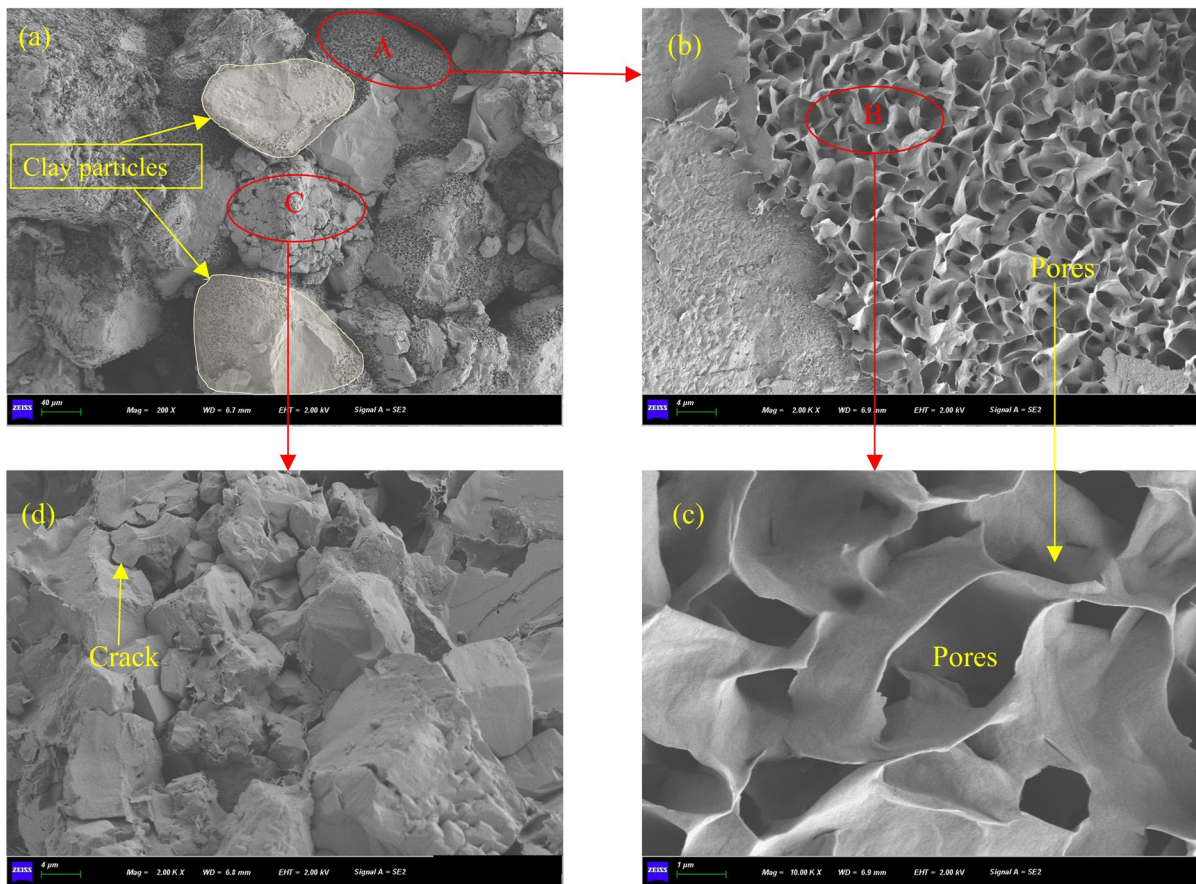
Fig. 4 Representative SEM images of argillaceous sandstone at normal temperature. **a** ×200; **b** ×2000; **c** ×10,000; **d** ×2000

is a small number of cracks distributed along the boundary of mineral particles.

Figure 5 presents part of the microstructure of argillaceous sandstone subjected to high treatment-temperature conditions. From 25 to 300 ℃, dehydration occurs inside the sample, and mineral particles do not expand significantly. At this time, the bearing capacity of the rock sample increases instead of decreasing. At 600 ℃, the mineral particles begin to expand, but there are still a large number of reticular cemented materials, indicating that the temperature has not caused a large amount of mineral decomposition, and the corresponding samples still have a considerable strength. From 900℃ to 1000℃, the expansion of mineral particles accelerates, the reticular cementation basically disappears, leading to the decrease of friction and cohesion between mineral particles, and the shape of mineral particles begins to change, indicating that at this time the mineral particles in a sample begin to

decompose, and the strength of the sample decreases rapidly. At 1200℃, the mineral particles partially melt, showing the characteristics of coarse and angular particle size, the adhesion between mineral particles further weaken, the pores gradually expand or even connect, and then form a network, and the strength of the sample greatly attenuates.

3.3 Analysis of LF-NMR results

According to the principles of LF-NMR testing, the transverse relaxation time T_2 can directly reflect pore structure. The T_2 distribution was first obtained by the inversion of the nuclear magnetic signals, then the pore size distribution was determined using the T_2 distributions. The relationship between T_2 and signal strength can be determined based on the attenuation of the measured echo (Kenyon 1992):
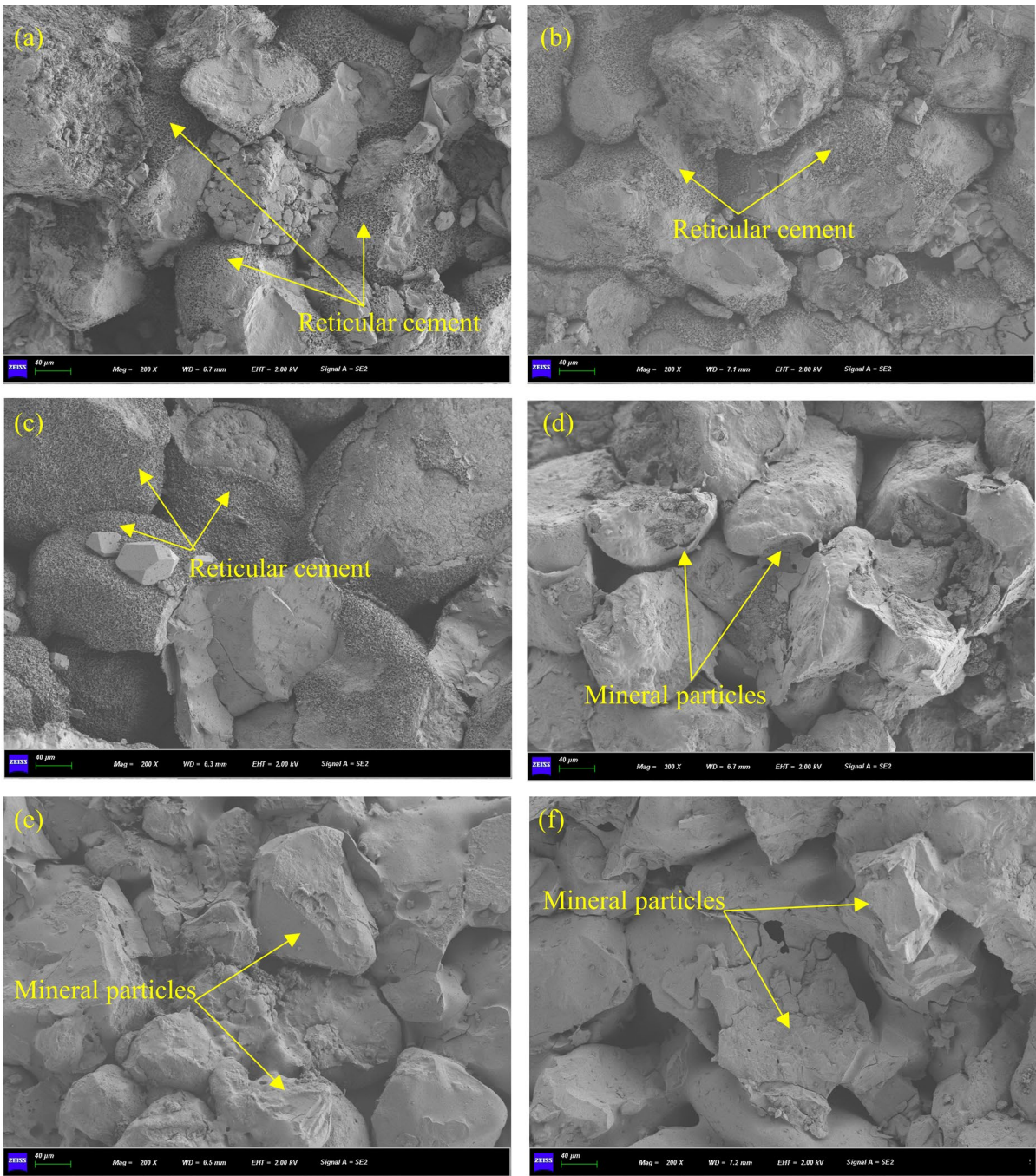
Fig. 5 SEM observations of argillaceous sandstone specimens after thermal treatment (×200): **a** 25 ℃; **b** 300 ℃; **c** 600 ℃; **d** 900 ℃; **e** 1000 ℃; **f** 1200 ℃
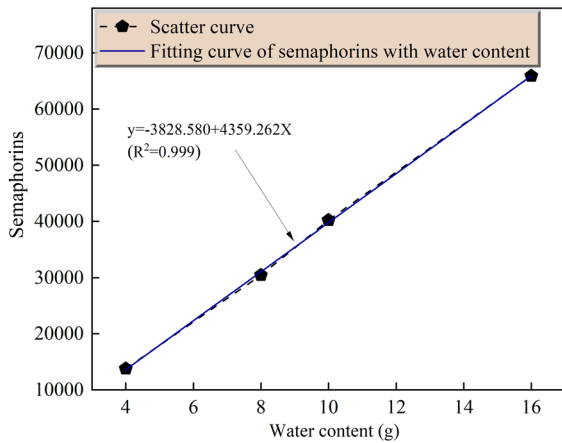
Fig. 6 Calibration curve of LF-NMR test

$$M(t) = M_0 e^{\left(-\frac{t}{T_2}\right)} \qquad (1)$$

where $M(t)$ is the echo signal amplitude corresponding to time t; M_0 is the echo signal amplitude corresponding to the initial time; T_2 is the transverse relaxation time, ms; t is the test time, ms. The T_2 is closely related to the surface area of the medium, so the expression of T_2 can be further obtained (Yao 2015):

$$\frac{1}{T_2} = \rho_2 \left(\frac{S_{pore}}{V_{pore}}\right) \qquad (2)$$

where ρ_2 is the transverse surface relaxation strength, μm/s; S_{pore} is the total pore surface area, μm^2; V_{pore} is the total pore volume, μm^3. It is assumed that the rock
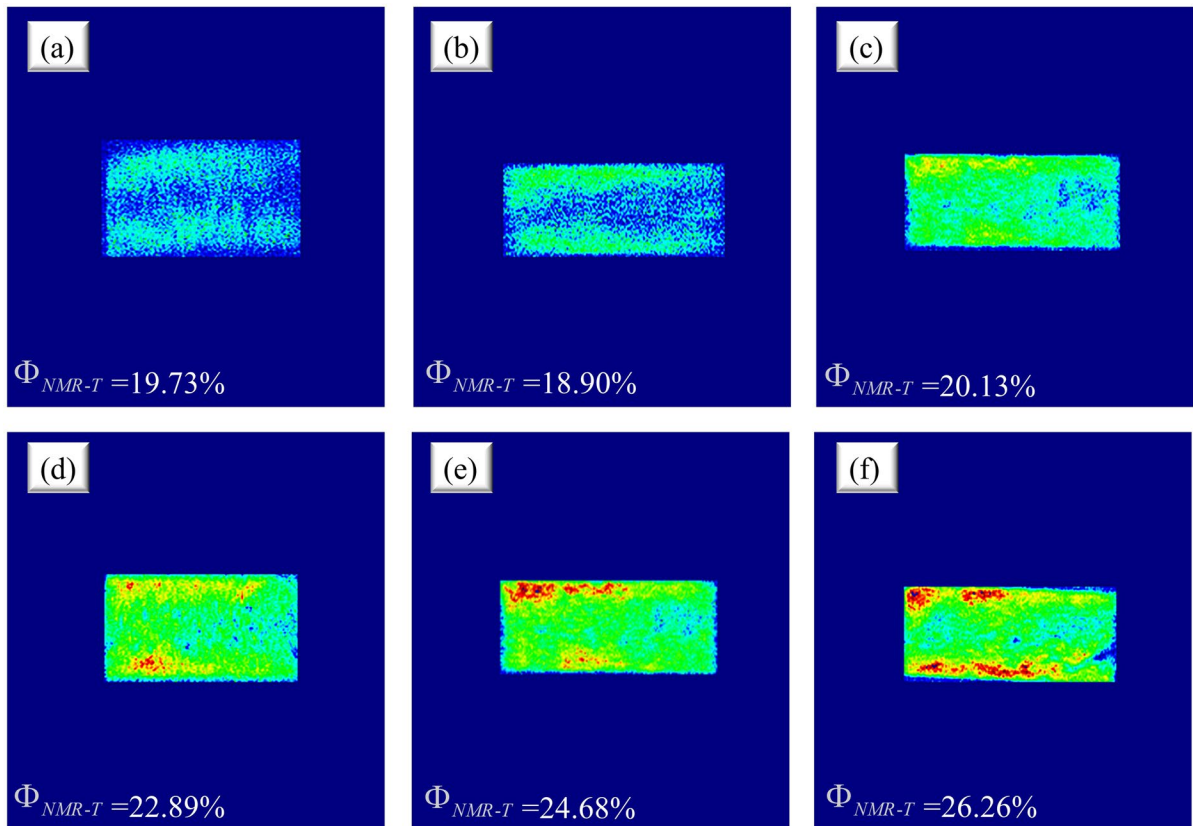
Fig. 7 LF-NMR images for argillaceous sandstone at different treatment temperatures: **a** 25 ℃; **b** 300 ℃; **c** 600 ℃; **d** 900 ℃; **e** 1000 ℃; **f** 1200 ℃

pore is a tube bundle model with a radius of r_{pore}, and $\rho_2 = 10$ μm/s. The pore size distribution can be obtained by inversion of the distribution:

$$r_{pore} = 0.2T_2 \tag{3}$$

Calibration was achieved by fitting a standard sample with known porosity to the nuclear magnetic signal per unit volume (Fig. 6).

LF-NMR images of the argillaceous sandstone after being subjected to different high-temperature treatments are presented in Fig. 7 (The procedure of testing and analysis of high-temperature samples is exactly the same as that of normal temperature samples). The bright area in the image is the area where the water molecules are located, and the brighter the color, the more water in the region. Figure 8 presented the LF-NMR T_2 spectrum distributions from the argillaceous sandstone samples subjected to different temperature temperatures. They can be divided into two types: bimodal and trimodal, and a right-bias bimodal type is common. For the normal temperature sample, the T_2 spectrum distribution range is 0.1–1000 ms and mainly composed of two peaks: the left peak is low, mainly located at 0.065–6.37 ms, and the right peak is steep and high, mainly located at 6.37–333.12 ms. The two peaks are interconnected, and the spectrum shape is narrow, indicating that the sample has low porosity and poor physical properties. When the treatment temperature is 300–900 °C, the curve shape of the T_2 spectrum distribution is similar to that under normal temperature and maintains a right-bias bimodal development. With the increase in heat treatment temperature, the curve shifts rightward and the pore connectivity appears to improve to a certain extent. A turning point emerges at a treatment temperature of 1000 °C, when the third peak appears in the T_2 spectrum distribution and the curve shifts upward. As the temperature increases further to 1200 °C, the curve recovers from three peaks to two peaks again. Hence, the high-temperature environment damaged the rock sample as reflected in the T_2 spectrum distribution curve; it did not lead to a significant right-shift in the curve but rather a large upward shift, indicating that the temperature does not substantially increase pore size but does increase the number of pores.

Figure 9 presents a histogram of the pore size distribution of samples for different treatment temperatures based on LF-NMR T_2 spectrum inversion. The division of pore scale directly affects the statistical analysis of pore test results, but there are no uniform requirements provided by classification standards. This paper uses two different detection methods, i.e., μ-CT and LF-NMR test. To facilitate comparative analysis, the pore size scale can be divided into three different ranges: small pores ($r_{pore} \leq 1\ \mu m$), medium pore ($1 < r_{pore} < 10\ \mu m$), and large pore ($r_{pore} \geq 10\ \mu m$). The statistics of the pore size distributions for different sample scales are presented in Table 2. Pore size changes after high-temperature treatments are very complicated, but some overall trends are evident. Small pores and medium pores consistently dominate the samples with pore volumes of 98.8–100%. Temperature affects the samples by free water dehydration, thermal expansion, organic
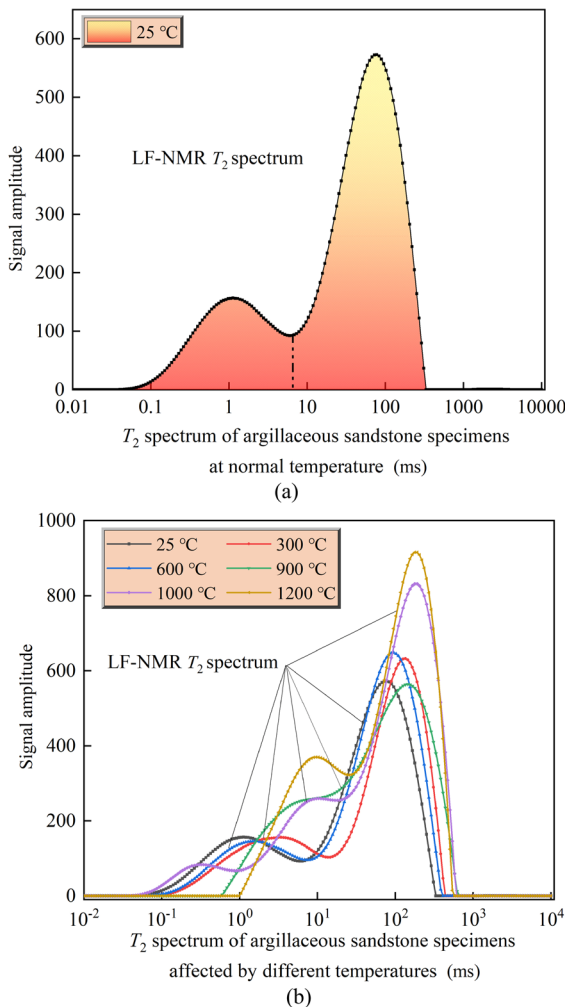

Fig. 8 LF-NMR T_2 spectrum distribution of argillaceous sandstone after thermal damage: **a** 25 ℃; **b** 25–1200 ℃

matter softening, and thermal decomposition of mineral components, but on the whole, under 1200ºC, small pores decrease as temperature increases while medium and large pores increase. To this effect, temperature causes the small pores to expand and develop into larger-scale pores, which in turn promotes the continuous deterioration of the sample. At 1200 °C, the decomposition of mineral components (mainly clay) in the sample is effectively complete. Ultra-high temperature appears to have caused the melting of some minerals and the blockage of some large pores.

3.4 Analysis of μ-CT results

A μ-CT density image of a sample was obtained by collecting the attenuation information of an X-ray after penetrating the sample. As can be seen in Fig. 10, a typical image gradually transitions from black to bright white, indicating a gradual increase in density from low to high. The black part represents low-density material, which usually characterizes pores of various scales. The bright white part represents high-density material, which usually characterizes the skeleton of the sample as mainly composed of various mineral particles and the cementation of organic or inorganic materials. Quantitative statistics of pores and high-density substances were gathered by threshold segmentation. The percentage of pores in the total volume reflects the porosity. The images qualitatively indicate certain pores in the samples at normal temperature that are dominated by high-density materials.
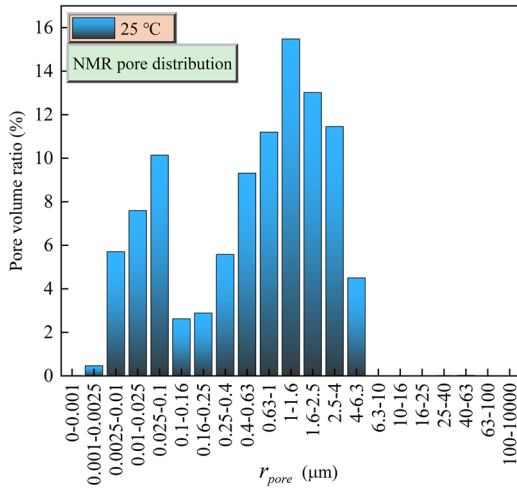
Digital core technology (Christe et al. 2011; Xia et al. 2020) is an effective means to examine the micro pore structures of rock cores via 3D visualization and quantitative characterization. As shown in Fig. 11, reconstructed 3D digital core pores were simplified and analyzed based on the maximum ball algorithm (Dong et al. 2009) to quantitatively extract pore radius information. The pore size distribution characteristics of rock samples subjected to different treatment temperatures are shown in Fig. 12. After different high-temperature treatments, the pore size distribution satisfies the normal distribution function and the fitting coefficients are generally greater than 0.94. Under normal temperature, the pore size distribution is in the range of 3–66 μm, the main distribution interval is 3 to 40 μm, and the cumulative distribution frequency reaches 98%. When the treatment temperature is 300–600 ºC, the pore size distribution does not significantly change.

When the treatment temperature reaches 900 ºC, the pore size distribution ranges from 2 to 88 μm. When the temperature reaches 1000–1200 ºC, the pore size distribution decreases in a range of 3–55 μm. These results are similar to the LF-NMR test results, as pore radius does not increase but decreases under the action of ultra-high temperature. The partitions of μ-CT test results are consistent with those of the LF-NMR results in terms of small pore ($r_{pore} \leq 1\ \mu m$), medium pore ($1 < r_{pore} < 10\ \mu m$), and large pore ($r_{pore} \geq 10\ \mu m$) ranges. The statistical pore size distribution information for different scales of sample is presented in Table 3. Considering the resolution of the μ-CT testing machine and the sample size, the final scanning resolution is 8.56 μm, hence there are some small pore sizes missing from the test results compared to the LF-NMR test. The distribution frequency of medium pores is 16.5% to 28.3% and the distribution frequency of large pores is 71.7% to 83.5%; large pores are obviously dominant. It appears that the μ-CT test results with a resolution of 10^1 μm do not capture the distribution information of some small pores in the argillaceous sandstone when medium and small pores dominate, and that the test does not fully reveal the micro pore structure of the samples.
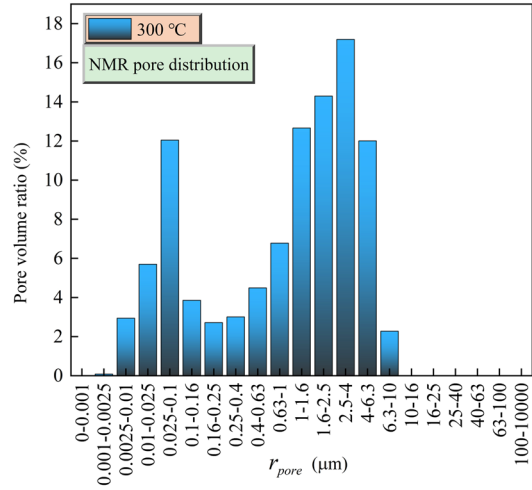
4 Discussion
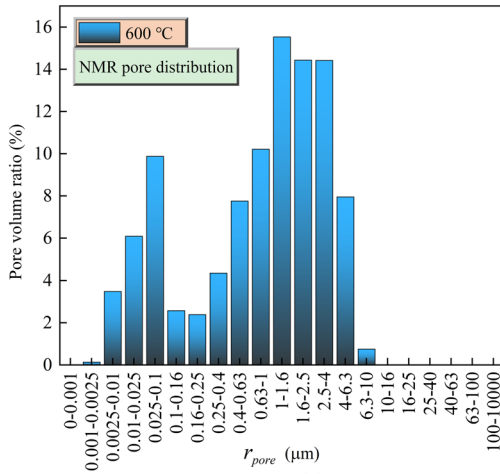
4.1 Changes in porosity

As the ratio of rock pore to rock volume, porosity is a key parameter related to rock pore structures. Porosity measurements largely depend on the test method and parameters utilized to gather them. Figure 13 presents the variations in porosity with treatment temperature based on the LF-NMR and μ-CT test results, and there are certain evident differences between them. The μ-CT porosity ranges from 11.1 to 15.2%, while LF-NMR porosity ranges from 18.9 to 26.3%. For the same treatment conditions, μ-CT porosity is generally smaller than LF-NMR porosity. The essence of the μ-CT test is to directly reflect the pore structure characteristics by the strength of X-ray absorption capacity of different substances in the sample, while that of the LF-NMR test is to indirectly reflect the pore structure characteristics by the water in the pores of the sample. Differences between the two sets of measurement results in this study can be attributed to two
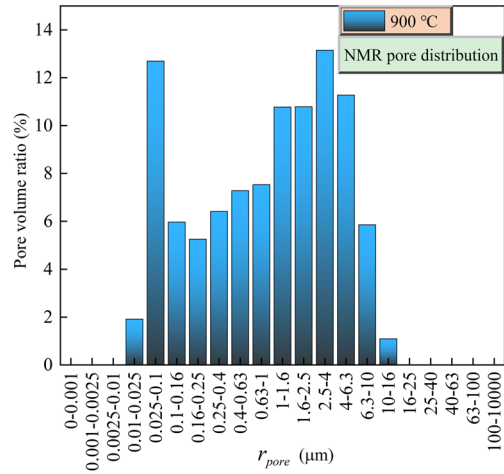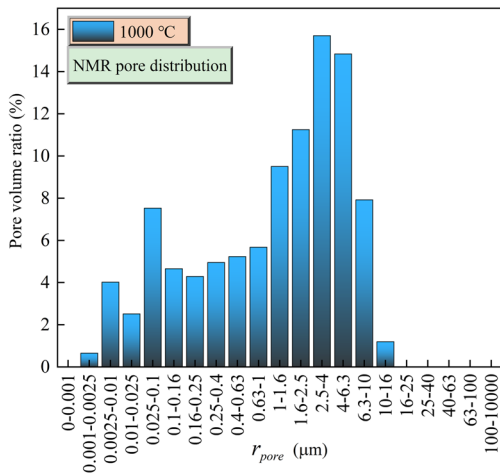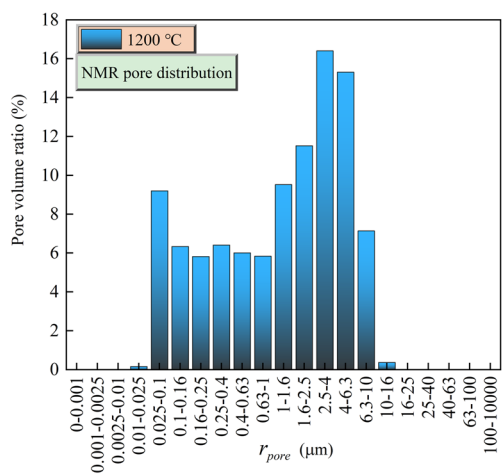
(a)

(b)

(c)

(d)

(e)

(f)

of rock materials to directly observe the pore space states and pore structure data.

According to our test results, the relation between porosities Φ_{NMR-T}, Φ_{CT-T} and temperature conforms to the following quadratic polynomial relation:

$$\begin{cases} \Phi_{NMR-T} = 19.578 - 3.440\left(\dfrac{T}{1000}\right) + 7.825\left(\dfrac{T}{1000}\right)^2 \ \left(R^2 = 0.979\right) \\ \Phi_{CT-T} = 12.007 - 1.830\left(\dfrac{T}{1000}\right) + 4.106\left(\dfrac{T}{1000}\right)^2 \ \left(R^2 = 0.881\right) \end{cases} \tag{4}$$

main factors. Firstly, because argillaceous sandstone contains a large number of clay matrix mineral particles, the clay easily absorbs water and swells. Moisture absorption in an LF-NMR test increases porosity but does not affect the attenuation of X-ray signals. When μ-CT test samples are dry, so the LF-NMR porosity is generally higher than the μ-CT porosity for the same treatment conditions. Secondly, due to the resolution of the test system and the sample size, theoretically speaking, pores larger than the scanning resolution can be identified by μ-CT while the LF-NMR test results are dominated by small and medium pores, and only some of these pores can discovered by μ-CT test. Hence the two test methods caused differences in the porosity results presented here, but the change trend of porosity with treatment temperature was the same for both methods. Both detection methods also demonstrate the effect of treatment temperature on the micro pore structure. As treatment temperature increases, the micro structure of the pores changes significantly and the overall porosity gradually increases.

LF-NMR and μ-CT testing technology have unique advantages and disadvantages in describing rock pore structures. LF-NMR is independent of the influence of the rock skeleton and reflects the distribution of pores at various scales in a more detailed and comprehensive manner, but for certain types of rock, LF-NMR technology cannot distinguish possible false pores and loses certain relevant details. The advantage of μ-CT scanning is that digital core technology displays the 3D distribution of pores in detail. However, it is limited by the resolution and may not reflect the influence of certain small pores. Micro pore structure analysis should rely on LF-NMR technology to measure the pore size distribution and be combined with μ-CT scanning to reconstruct the 3D structure

where Φ_{NMR-T} is the porosity of rock samples after temperature treatment based on the LF-NMR test; and Φ_{CT-T} is the porosity of rock samples after temperature treatment based on the μ-CT test.

4.2 Changes in damage

A high-temperature environment promotes the initiation, development, and expansion of pores in rock materials in a process of damage evolution. The thermal damage variable of rock defined by porosity can be written as follows:

$$\Delta_T = \Phi'_T \big/ \left(1 - \Phi_N\right) \tag{5}$$

where Δ_T is the thermal damage variable of the rock under the action of temperature T; Φ'_T is the induced porosity of rock at temperature T, %; and Φ_N is the initial porosity of rock at temperature T, %. The induced porosity can be expressed as:

$$\Phi'_T = \Phi_T - \Phi_N \tag{6}$$

where Φ_T is the porosity of rock samples after high temperature treatment based on different testing techniques.

The thermal damage variable expressed in terms of porosity can be expressed by combining Eqs. (5) and (6):

$$\Delta_T = \left(\Phi_T - \Phi_N\right) \big/ \left(1 - \Phi_N\right) \tag{7}$$

According to the LF-NMR and μ-CT test results, the relationship between thermal damage and treatment temperature in argillaceous sandstone after high-temperature treatment can be obtained by fitting the following relation:

Table 2 Statistics of LF-NMR test results

Sample No	Temperature T (℃)	Percentage of small pores (%)	Percentage of medium pores (%)	Percentage of large pores (%)	Φ_{NMR-T}(%)	Δ_{NMR-T}(%)
B-1–1	25	55.51	44.44	0.05	19.73	0.00
B-2–1	300	41.59	58.41	0.00	18.90	−1.04
B-3–2	600	46.89	53.09	0.02	20.13	0.50
B-4–3	900	47.06	51.84	1.10	22.89	3.94
B-5–3	1000	39.58	59.22	1.20	24.68	6.17
B-6–1	1200	39.75	59.88	0.37	26.26	8.13
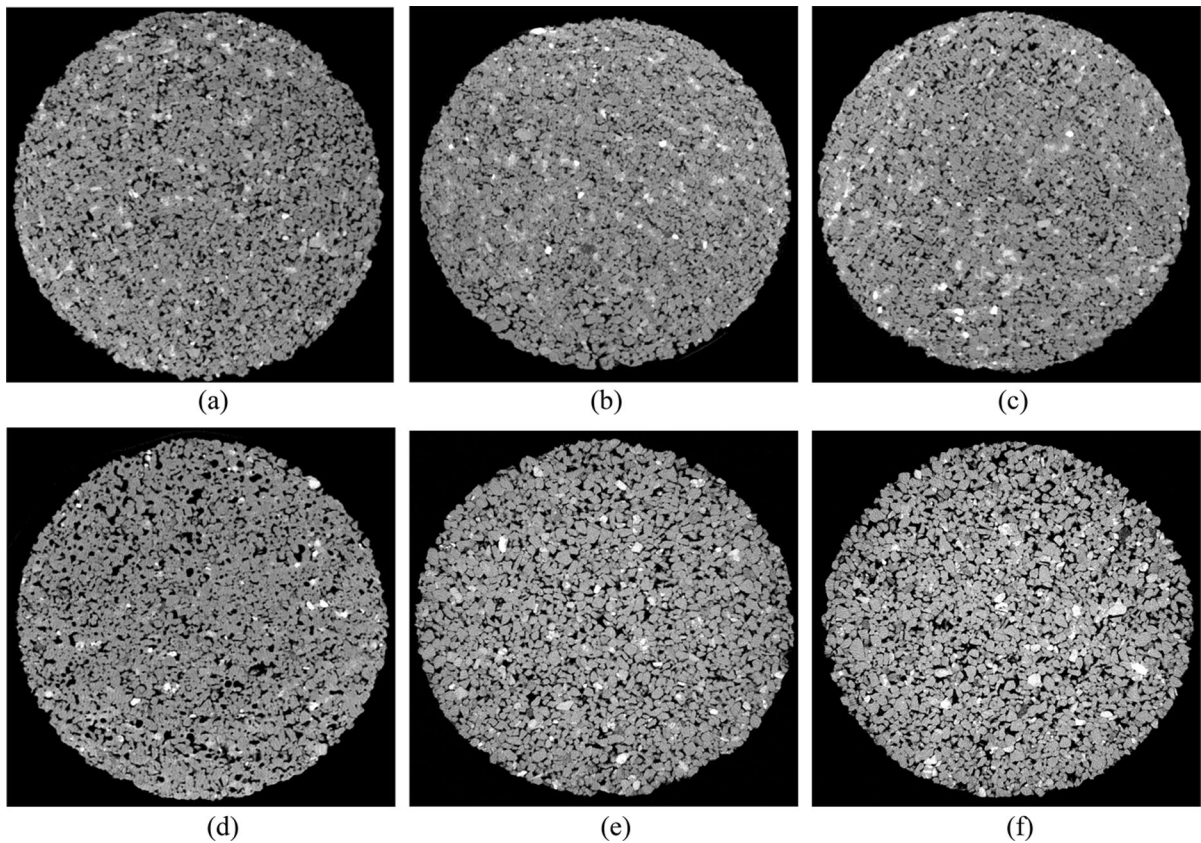
Fig. 10 μ-CT images of argillaceous sandstone specimens at different temperatures: **a** 25 ℃; **b** 300 ℃; **c** 600 ℃; **d** 900 ℃; **e** 1000 ℃; **f** 1200 ℃

$$\begin{cases} \Delta_{NMR-T} = -0.190 - 4.280\left(\dfrac{T}{1000}\right) + 9.748\left(\dfrac{T}{1000}\right)^2 & \left(R^2 = 0.979\right) \\[2mm] \Delta_{CT-T} = 0.437 - 2.090\left(\dfrac{T}{1000}\right) + 4.687\left(\dfrac{T}{1000}\right)^2 & \left(R^2 = 0.881\right) \end{cases} \tag{8}$$

Fig. 11 3D reconstruction of pore structure of argillaceous sandstone specimens at different temperatures: **a** 25 ℃; **b** 300 ℃; **c** 600 ℃; **d** 900 ℃; **e** 1000 ℃; **f** 1200 ℃
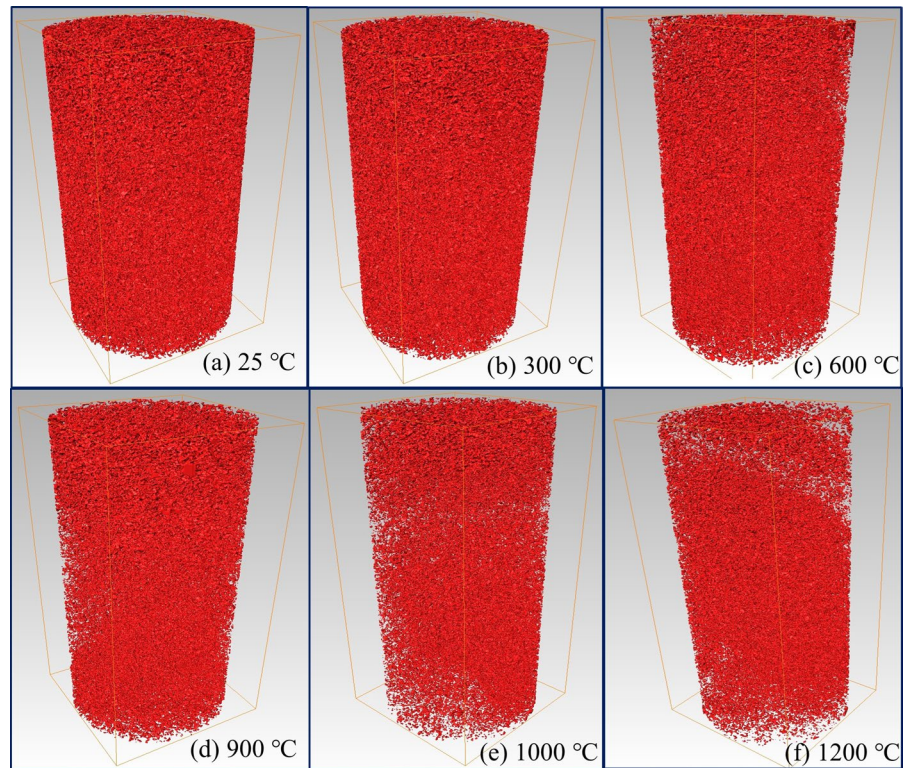
where Δ_{NMR-T} is the thermal damage variable of rock samples after temperature treatment based on the LF-NMR test; and Δ_{CT-T} is the thermal damage variable of rock samples after temperature treatment based on the μ-CT test.

The correlation coefficients in this case reach 0.979 and 0.881, respectively. This relation can be used to predict the change in argillaceous sandstone thermal damage after different high-temperature treatments. According to the curves of thermal damage and temperature (Fig. 14), the thermal damage calculated by either test technique shows a non-linear relationship with temperature. Although the magnitude of the damage is somewhat different between the two techniques, the evolution trends are basically the same. Under normal temperature, both thermal damage values are 0. When the treatment temperature rises to 300 ℃, both Δ_{NMR-T} and Δ_{CT-T} become negative values at -1.0% and − 1.5%, respectively. To this effect, temperature not only degrades the rock but also strengthens it.

The mechanical test results confirmed that 300 ℃ is likely to be the threshold temperature for the change of the high-temperature mechanical nonlinear behavior of argillaceous sandstone. The damage results defined by the porosity obtained by the microscopic testing methods also reflect this result, which suggests the validity of the macroscopic mechanical test and also shows that the thermal damage defined by the porosity can reflect the mechanical results to a certain extent. There is consistency between macroscopic tests and microscopic tests. It is possible that treatment temperatures of 300 °C cause the moisture in the pores to evaporate, improving the physical properties of the pores while decreasing porosity. As treatment temperature is increased, both Δ_{NMR-T} and Δ_{CT-T} gradually increase though there is a difference in the magnitude of increase between the two test techniques. At 1200 ℃, Δ_{NMR-T} and Δ_{CT-T} are 8.1% and -3.2%, respectively. According to the thermal damage curve, the argillaceous sandstone experienced evolution through strengthening, damage derivation, and damage development as treatment temperature is increased. Therefore, thermal damage variables defined based on porosity can scientifically describe the rock damage evolution mechanism during temperature rise.
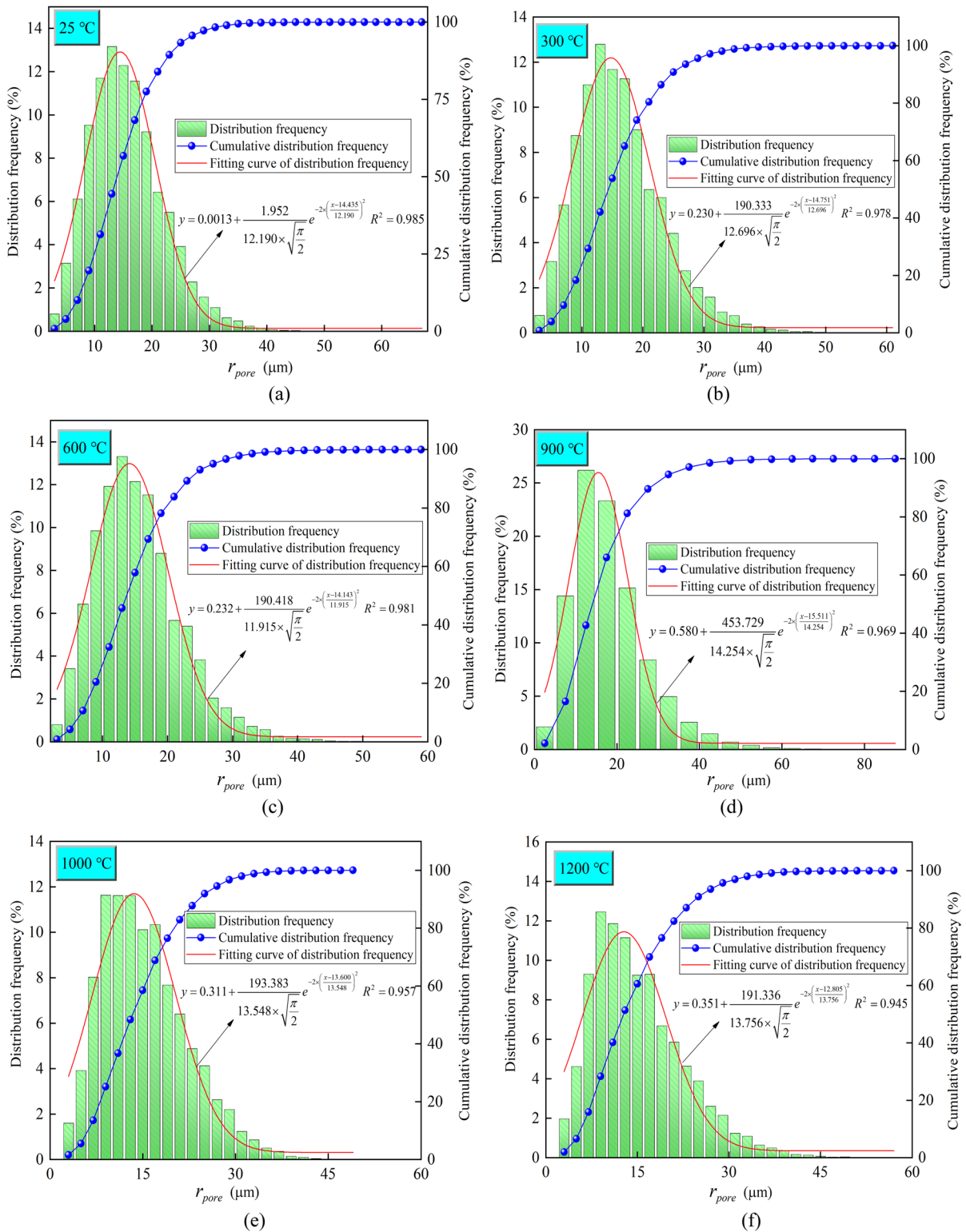
Fig. 12 Pore size distribution characteristics of argillaceous sandstone based on μ-CT technology: **a** 25 ℃; **b** 300 ℃; **c** 600 ℃; **d** 900 ℃; **e** 1000 ℃; **f** 1200 ℃

Table 3 Statistics of μ-CT test results

Sample No	Temperature T (℃)	Percentage of small pores (%)	Percentage of medium pores (%)	Percentage of large pores (%)	Φ_{CT-T}(%)	Δ_{CT-T}(%)
C-1–1	25	0	19.59	80.41	12.39	0.00
C-2–3	300	0	18.35	81.65	11.08	−1.50
C-3–1	600	0	20.50	79.50	12.26	−0.15
C-4–3	900	0	16.52	83.48	14.15	2.01
C-5–1	1000	0	25.17	74.83	14.84	2.80
C-6–2	1200	0	28.34	71.66	15.16	3.16
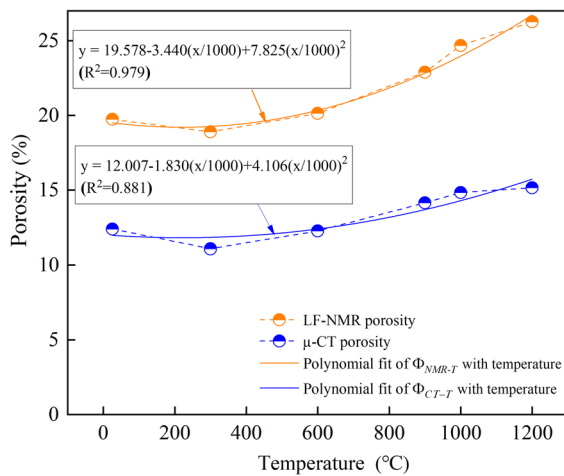
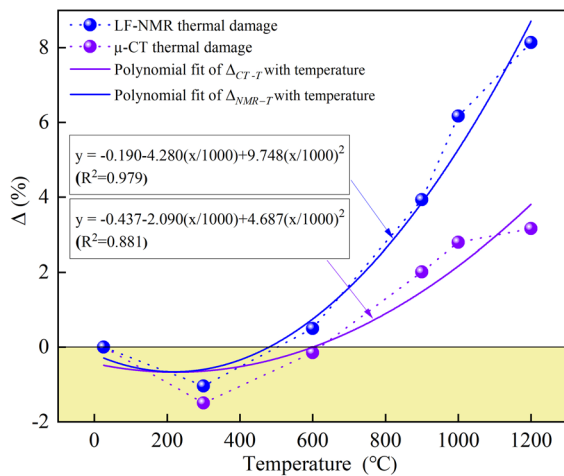**Fig. 13** Curve of porosity vs temperature

Fig. 14 Curve of thermal damage variable vs temperature

5 Conclusions

1. Based on the uniaxial compression test results of argillaceous sandstone after high-temperature treatment, it is found that with increasing treatment temperature, the variation trends of peak stress and elastic modulus are basically the same, which an increase first and then a decrease, while the peak strain decreases first and then increases. The three mechanical parameters all suggest that 300 ℃ is probably the threshold temperature for the high-temperature nonlinear mechanical behavior of argillaceous sandstone. According to the SEM results, under 300 ℃ treatment, high-temperature causes mineral shrinkage by evaporating part of water, which results in a strengthening effect. Above 300 ℃, the high-temperature will lead to the expansion of mineral particles, resulting in dominant weakening effects.

2. According to LF-NMR test results, the T_2 spectrum of high-temperature treated argillaceous sandstone may be bimodal or trimodal. The right-biased bimodal type is typical and common among different samples. Pore size variations are very complex but show some overall trends. Small and medium pores consistently dominate and have pore volumes of 98.8–100%. Under 1200 ℃, small pores decrease with temperature while medium and large pores gradually increase. At 1200 ℃, the super high-temperature melts certain minerals and blocks a portion of the large pores, resulting in a decrease in large pores.

3. According to the μ-CT test results, the pore size distribution satisfies the normal function and the

fitting coefficients are generally greater than 0.94. Under normal temperature, the pore size distribution is between 3 and 66 μm, the main interval is 3 to 40 μm, and the cumulative distribution frequency reaches 98%. When treatment temperature is 300–600 ℃, the pore size distribution does not markedly change. When treatment temperature reaches 900℃, the pore size distribution ranges from 2 to 88 μm. When treatment temperature is 1000–1200 ℃, the pore size distribution does not increase but rather decreases and the range is 3–55 μm. These results are similar to the LF-NMR test results, where large pores do not increase but rather decrease under the action of super high-temperature.

4. The μ-CT porosity ranges from 11.1 to 15.2% and the LF-NMR porosity ranges from 18.9–26.3%. Under the same conditions, the μ-CT porosity is generally smaller than the LF-NMR porosity. Numerous clay matrix mineral particles in the argillaceous sandstone easily absorb water and expand, which causes a porosity increase in an LF-NMR test. In μ-CT tests, water absorption does not affect X-ray signal attenuation. The limited test system resolution also causes the μ-CT test to lose some pores. Although the results of the two methods are different, the porosity variation trends with temperature revealed by the two tests are consistent. Both methods can reflect temperature effects in pore structures.

5. A thermal damage evolution equation was established based on the porosity information gathered in the tests. The thermal damage calculated by both techniques showed a nonlinear relationship with temperature. The damage variables are different but the evolution trends are basically the same. At normal temperature, the two thermal damage values are 0; when temperature rises to 300 ℃, both Δ_{NMR-T} and Δ_{CT-T} become negative at − 1.04% and -1.50%, respectively, indicating that temperature not only degrades the rock but also strengthens it. There is consistency between macroscopic tests and microscopic tests. With further increase in temperature, Δ_{NMR-T} and Δ_{CT-T} gradually increase but across different ranges for the two test methods. At 1200 ℃, Δ_{NMR-T} and Δ_{CT-T} are 8.1% and − 3.2%, respectively. The thermal damage variation curve indicates that argillaceous sandstone evolves through

stages of strengthening, damage derivation, and damage development as treatment temperature is increased.

Declarations

References

Adeyilola A, Nordeng S, Onwumelu C, Nwachukwu F, Gentzis T (2020) Geochemical, petrographic and petrophysical characterization of the Lower Bakken Shale, Divide County. North Dakota Int J Coal Geol 224:103477

Bandara K, Ranjith PG, Haque A, Wanniarachchi WAM, Zheng W, Rathnaweera TD (2021) An experimental investigation of the effect of long-term, time-dependent proppant embedment on fracture permeability and fracture aperture reduction. Int J Rock Mech Min Sci 144:104813

Chang Y, Yao Y, Liu Y, Zheng S (2020) Can cuttings replace cores for porosity and pore size distribution analyses of coal. Int J Coal Geol 227:103534

Christe P, Turberg P, Labiouse V, Meuli R, Parriaux A (2011) An X-ray computed tomography-based index to characterize the quality of cataclastic carbonate rock samples. Eng Geol 117(3–4):180–188

Das D, Mishra B, Gupta N (2021) Understanding the influence of petrographic parameters on strength of differently sized shale specimens using XRD and SEM. Int J Min Sci Techno 31:953–961

Ding CD, Hu DW, Zhou H, Lu JJ, Lv T (2020) Investigations of P-Wave velocity, mechanical behavior and thermal

properties of anisotropic slate. Int J Rock Mech Min Sci 127:104176

Dong H, Blunt MJ (2009) Pore-network extraction from micro-computerized-tomography images. Phys Rev E 80(3):036307

Ebadi M, Orlov D, Makhotin I, Krutko V, Belozerov B, Koroteev D (2021) Strengthening the digital rock physics, using downsampling for sub-resolved pores in tight sandstones. J Nat Gas Sci Eng 89:103869

Habina I, Radzik N, Topor T, Krzyzak AT (2017) Insight into oil and gas-shales compounds signatures in low field H-1 NMR and its application in porosity evaluation. Microporous Mesoporous Mater 252:37–49

Hao Z, Zuo Y, Liu H, Zhu Z, Lin J, Sun W, Pan C, Zheng L (2022) Mesoscopic damage evolution characteristics of jointed sandstone under different loading conditions. Geomech Geophys Geo-Energ Geo-Resour 8:92

Hashan M, Munshi TA, Zaman A, Jahan LN (2022) Empirical, statistical, and connectionist methods coupled with log variables ranking for the prediction of pore network permeability in a heterogeneous oil reservoir. Geomech Geophys Geo-Energ Geo-Resour 8:117

ISRM (2007) The complete ISRM suggested methods for rock characterization, testing and monitoring: 1974–2006. In: Ulusay, Hudson (Eds.), Suggested methods prepared by the commission on testing methods, International Society for Rock Mechanics. ISRM Turkish National Group, Ankara, Turkey. 628 pp

Jiang HP, Jiang AN, Zhang FR (2020) Comparative experimental study on the physical and mechanical properties of quartz sandstone after water-cooling and natural-cooling under high temperature. Q J Eng Geol Hydrogeol qjegh2020–181

Kahraman E (2022) Investigation of the effects of two different cooling treatments on the physico-mechanical and microstructural properties of granite after high temperatures. Geomech Geophys Geo-Energ Geo-Resour 8:142

Kang FC, Li YC, Tang CA (2021) Grain size heterogeneity controls strengthening to weakening of granite over high-temperature treatment. Int J Rock Mech Min Sci 145:104848

Katika K, Fordsmand H, Fabricius IL (2018) Low field NMR surface relaxivity studies of chalk and argillaceous sandstones. Microporous Mesoporous Mater 269:122–124

Kenyon WE (1992) Nuclear magnetic resonance as a petrophysical measurement. Nucl Geophys 6:153–171

Kim G, Jang J, Kim KY, Yun TS (2020) Characterization of orthotropic nature of cleavage planes in granitic rock. Eng Geol 265:105432

Kumari WGP, Ranjith PG, Perera MSA, Li X, Li LH, Chen BK, Isaka BLA, De Silva VRS (2018) Hydraulic fracturing under high temperature and pressure conditions with micro CT applications: geothermal energy from hot dry rocks. Fuel 230:138–154

Li Z, Wu SH, Xia DL, He SC, Zhang XF (2018) An investigation into pore structure and petrophysical property in tight sandstones: a case of the Yanchang formation in the southern Ordos Basin. Chinan Mar Petrol Geol 97:390–406

Li M, Wang D, Shao Z (2020) Experimental study on changes of pore structure and mechanical properties of sandstone after high-temperature treatment using nuclear magnetic resonance. Eng Geol 275:105739

Li ZG, Xu GL, Dai YY, Zhao X, Fu YP (2021) Effects of foliation on deformation and failure mechanism of silty slates. Int J Rock Mech Min Sci 141:104703

Li D, Su X, Gao F, Liu Z (2022) Experimental studies on physical and mechanical behaviors of heated rocks with pre-fabricated hole exposed to different cooling rates. Geomech Geophys Geo-Energ Geo-Resour 8:125

Liang K, Xie LZ, He B, Zhao P, Zhang Y, Hu WZ (2021) Effects of grain size distributions on the macro-mechanical behavior of rock salt using micro-based multiscale methods. Int J Rock Mech Min Sci 138:104592

Liu S, Xu JY (2014) Mechanical properties of Qinling biotite granite after high temperature treatment. Int J Rock Mech Min Sci 71:188–193

Liu S, Xu JY (2015) An experimental study on the physico-mechanical properties of two post-high-temperature rocks. Eng Geol 185:63–70

Liu JR, Li BY, Tian W, Wu XR (2018) Investigating and predicting permeability variation in thermally cracked dry rocks. Int J Rock Mech Min Sci 103:77–88

Liu K, Ostadhassan M, Sun L, Zou J, Yuan Y, Gentzis T, Zhang Y, Ortiz HC, Rezaee R (2019) A comprehensive pore structure study of the Bakken Shale with SANS, N2 adsorption and mercury intrusion. Fuel 245:274–285

Lyu C, Hao SQ, Sun Q, Zhang WQ, Geng JS (2021) Permeability evolution of two sedimentary rocks at different temperatures based on the Katz-Thompson theory. Int J Rock Mech Min Sci 144:104819

Ma X, Wang GL, Hu DW, Liu YG, Zhou H, Liu F (2020) Mechanical properties of granite under real-time high temperature and three-dimensional stress. Int J Rock Mech Min Sci 136:104521

Ma TS, Zhu GS, Peng N, Qiu Y, Liu Y, Zou JY (2021) Physical-mechanical properties and thermal-induced damage of granite after high-temperature pretreatment. Arabian J Geosci 14:1449

Martinez-Ibanez V, Garrido ME, Signes CH, Tomas R (2021) Micro and macro-structural effects of high temperatures in Prada limestone: key factors for future fire-intervention protocols in tres ponts tunnel (Spain). Constr Build Mater 286:122960

Meng FZ, Song J, Wong LNY, Wang ZQ, Zhang CQ (2021) Characterization of roughness and shear behavior of thermally treated granite fractures. Eng Geol 293:106287

Pathiranagei SV, Gratchev I, Kong R (2021) Engineering properties of four different rocks after heat treatment. Geomech Geophys Geo-Energ Geo-Resour 7:16

Ranjith PG, Viete DR, Chen BJ, Perera MSA (2012) Transformation plasticity and the effect of temperature on the mechanical behaviour of Hawkesbury sandstone at atmospheric pressure. Eng Geol 151:120–127

Romero-Sarmiento MF, Ramirez SR, Berthe G, Fleury M, Littke R (2017) Geochemical and petrophysical source rock characterization of the Vaca Muerta formation, Argentina: implications for unconventional petroleum resource estimations. Int J Coal Geol 184:27–41

Sun Q, Zhang WQ, Xue L, Zhang ZZ, Su TM (2015) Thermal damage pattern and thresholds of granite. Environ Earth Sci 74:2341–2349

Sun W, Wu SC, Xu XL (2021) Mechanical behaviour of Lac du Bonnet granite after high-temperature treatment using bonded-particle model and moment tensor. Comput Geotech 135:104132

Wang Y, Sun S (2021) Multiscale pore structure characterization based on SEM images. Fuel 289:119915

Wang F, Fruhwirt T, Konietzky H (2020) Influence of repeated heating on physical-mechanical properties and damage evolution of granite. Int J Rock Mech Min Sci 136:104514

Wang Y, Zhu C, He M, Wang X, Le H (2022) Macro-meso dynamic fracture behaviors of Xinjiang marble exposed to freeze thaw and frequent impact disturbance loads: a lab-scale testing. Geomech Geophys Geo-Energ Geo-Resour 8:154

Wu Y, Li X-Z, Huang Z, Wang Y-C, Deng L-C (2021a) Effect of thermal damage on tensile strength and microstructure of granite: a case study of Beishan. China Geomech Geophys Geo-Energ Geo-Resour 7:82

Wu Y, Li XZ, Huang Z, Xue S (2021b) Effect of temperature on physical, mechanical and acoustic emission properties of Beishan granite, Gansu Province. China Nat Hazards 107:1577–1592

Xia Y, Zhang C, Zhou H, Chen J, Gao Y, Liu N, Chen P (2020) Structural characteristics of columnar jointed basalt in drainage tunnel of Baihetan hydropower station and its influence on the behavior of P-wave anisotropy. Eng Geol 264:105304

Xiao Q, Yang Y, Jiang B, Zhao X, Yu R, Liu Z, Wang H (2021) Evaluation method of the micro-occurrence and utilization patterns of gas via a novel method based on nuclear magnetic resonance. J Nat Gas Sci Eng 86:103721

Xu J, Kang Y, Hu Y, Liu F, Wang Z, Wang X (2021) Effects of hydrothermal treatment on dynamic properties of granite containing single fissure subject to impact loading. Geomech Geophys Geo-Energ Geo-Resour 7:32

Yao YB, Liu DM, Liu JG, Xie SB (2015) Assessing the water migration and permeability of large intact bituminous and anthracite coals using NMR relaxation spectrometry. Transp Porous Media 107:527–542

Yu C, Tian W, Zhang CS, Chai SB, Cheng X, Wang XH (2021) Temperature-dependent mechanical properties and crack propagation modes of 3D printed sandstones. Int J Rock Mech Min Sci 146:104868

Yuan Y, Rezaee R, Yu H, Zou J, Liu K, Zhang Y (2021) Compositional controls on nanopore structure in different shale lithofacies: a comparison with pure clays and isolated kerogens. Fuel 303:121079

Zhang F, Zhang YH, Yu YD, Hu DW, Shao JF (2020) Influence of cooling rate on thermal degradation of physical and mechanical properties of granite. Int J Rock Mech Min Sci 129:104285

Zhao YS, Wan ZJ, Feng ZJ, Xu ZH, Liang WG (2017) Evolution of mechanical properties of granite at high temperature and high pressure. Geomech Geophys Geo-Energ Geo-Resour 3:199–210

Zhao Y, Peng L, Liu S, Cao B, Sun Y, Hou B (2019) Pore structure characterization of shales using synchrotron SAXS and NMR cryoporometry. Mar Petrol Geol 102:116–125

Zhao F, Sun Q, Zhang WQ (2020a) Quantitative analysis of the influence of temperature and confining pressure on brittleness of granite: a review. Acta Geodynamica Et Geomaterialia 17:39–50

Zhao Y, Liu T, Danesh NN, Sun Y, Liu S, Wang Y (2020b) Quantification of pore modification in coals due to pulverization using synchrotron small angle X-ray scattering. J Nat Gas Sci Eng 84:103669

Zhou HW, Zhong JC, Ren WG, Wang XY, Yi HY (2018) Characterization of pore-fracture networks and their evolution at various measurement scales in coal samples using X-ray μCT and a fractal method. Int J Coal Geol 189:35–49

Zhu F, Hu WX, Cao J, Sun FN, Liu YF, Sun ZM (2018) Micro/nanoscale pore structure and fractal characteristics of tight gas sandstone: A case study from the Yuanba area, Northeast Sichuan Basin. China Mar Petrol Geol 98:116–132